

# A Low-Resolution Image is Worth 1x1 Words: Enabling Fine Image Super-Resolution with Transformers and TaylorShift

Sanath B Nagaraju<sup>1</sup>, Brian B Moser<sup>1,2,3</sup>, Tobias C Nauen<sup>1,2</sup>, Stanislav Frolov<sup>2</sup>,  
Federico Raue<sup>2</sup>, and Andreas Dengel<sup>1,2</sup>

<sup>1</sup> University of Kaiserslautern-Landau, Germany

<sup>2</sup> German Research Center for Artificial Intelligence, Germany

<sup>3</sup> Corresponding Author

`first.last@dfki`

**Abstract.** Transformer-based architectures have recently advanced the image reconstruction quality of super-resolution (SR) models. Yet, their scalability remains limited by quadratic attention costs and coarse patch embeddings that weaken pixel-level fidelity. We propose TaylorIR, a plug-and-play framework that enforces  $1 \times 1$  patch embeddings for true pixel-wise reasoning and replaces conventional self-attention with TaylorShift, a Taylor-series-based attention mechanism enabling full token interactions with near-linear complexity. Across multiple SR benchmarks, TaylorIR delivers state-of-the-art performance while reducing memory consumption by up to 60%, effectively bridging the gap between fine-grained detail restoration and efficient transformer scaling.

**Keywords:** Image Super-Resolution · Vision Transformers · TaylorShift.

## 1 Introduction

Image super-resolution (SR) aims to recover high-resolution (HR) images from low-resolution (LR) inputs, restoring visual detail that is often critical in domains such as security, medical imaging, and remote sensing [11, 20, 21, 26, 28]. Despite recent progress, SR remains challenging, particularly in reconstructing high-frequency details that define texture and sharpness [9, 14, 19].

Early SR methods based on convolutional neural networks (CNNs) achieved strong results by learning hierarchical image features [13, 32, 34]. More recently, transformer-based models have surpassed CNNs by capturing long-range dependencies and richer contextual relationships [3, 6, 12, 25, 29, 31]. These architectures leverage self-attention mechanisms that model interactions across spatial tokens, leading to superior restoration quality.

However, transformer-based SR still faces two main limitations: high computational cost and loss of fine spatial detail. First, the *quadratic cost of self-attention* restricts how large an image the model can process at once. To stay feasible, most methods limit attention to small *windows* (e.g.,  $8 \times 8$  tokens), so each token



Fig. 1: Overview of TaylorIR’s impact on image SR. Using  $1 \times 1$  patch embeddings, TaylorIR models the image at pixel-level resolution. TaylorShift [22] replaces standard self-attention with a Taylor-series-based alternative that maintains full token interaction while reducing memory load.

only interacts with a small neighborhood instead of the entire image. Second, SR transformers often group pixels into larger *patches* (e.g.,  $4 \times 4$  or  $8 \times 8$ ), which reduces sequence length but also averages out local variations. As a result, small windows and large patches restrict long-range reasoning and blur fine details.

To overcome these challenges, we introduce TaylorIR, a transformer-based SR framework that enables pixel-level reasoning while remaining efficient. TaylorIR replaces conventional self-attention with TaylorShift [22], a memory-efficient mechanism derived from Taylor series expansion. It approximates full token-to-token attention with near-linear complexity, making large-scale, per-pixel attention feasible. For Swin-based SR architectures, we develop TaylorSwinIR, which extends SwinIR to use  $1 \times 1$  patches and larger attention windows, scaling from  $8 \times 8$  (64 tokens) to  $48 \times 48$  (2304 tokens), without prohibitive memory growth. TaylorShift enables this expansion, allowing global context modeling and sharper detail recovery. Compared to baseline SwinIR, TaylorIR achieves higher PSNR and SSIM across multiple benchmarks while cutting memory usage by up to 60%, as demonstrated empirically in extensive experiments across standard benchmarks and exemplified in Figure 1.

Our main contributions are:

- **Pixel-Level Patch Embedding:** We introduce a  $1 \times 1$  patch embedding strategy that enables transformers to operate directly on pixels, enhancing fine-grained reconstruction.
- **TaylorShift Attention:** A Taylor-series-based approximation that achieves global token interaction with near-linear complexity and reduced memory footprint.
- **Improved SR Performance and Efficiency:** TaylorSwinIR consistently outperforms current SR transformers across standard datasets, offering a stronger balance between reconstruction quality and computational efficiency.

## 2 Background: Self-Attention

In transformers [7, 25], the attention mechanism determines how strongly each token in a sequence relates to every other token. For a sequence of length  $N$ , standard self-attention computes pairwise interactions between all tokens, enabling global context modeling but at a quadratic computational cost.

The process involves three main steps:

1. **Query–Key Similarity:** Compute pairwise affinities between queries  $Q$  and keys  $K$ :

$$A = QK^\top \in \mathbb{R}^{N \times N}. \quad (1)$$

2. **Softmax Normalization:** Convert similarities into normalized weights:

$$\text{softmax}(A)_{ij} = \frac{\exp(A_{ij})}{\sum_k \exp(A_{ik})}. \quad (2)$$

3. **Value Aggregation:** Weight the value matrix  $V$  using the attention scores:

$$Y = \text{softmax}(A)V. \quad (3)$$

Overall, the time complexity of classical self-attention is  $\mathcal{O}(N^2d)$ , which becomes computationally expensive, particularly for long sequences.

## 3 TaylorIR

TaylorIR is a simple drop-in recipe to make transformer SR both *finer* and *leaner*. It has two parts: (i) TaylorShift attention to keep long-range interactions affordable in time and memory, and (ii) pixel-wise patch embedding ( $1 \times 1$ ) to let the model reason at the level of individual pixels.

### 3.1 TaylorShift Attention

TaylorShift replaces the softmax in attention with a low-order Taylor expansion. It keeps the expressiveness of full token-to-token interactions while reducing runtime and memory.

**Direct TaylorShift** Let  $A = QK^\top \in \mathbb{R}^{N \times N}$ . Direct TaylorShift uses a second-order Taylor approximation of the exponential and normalizes it to a valid distribution:

$$\text{T-SM}(A)_{ij} = \frac{1 + A_{ij} + \frac{1}{2}A_{ij}^2}{\sum_k (1 + A_{ik} + \frac{1}{2}A_{ik}^2)}. \quad (4)$$

The output is then  $Y = \text{T-SM}(A)V$ . This avoids exponentials and is slightly faster than softmax, but it still has the same asymptotic cost,  $\mathcal{O}(N^2d)$ , because it forms and uses the  $N \times N$  matrix.

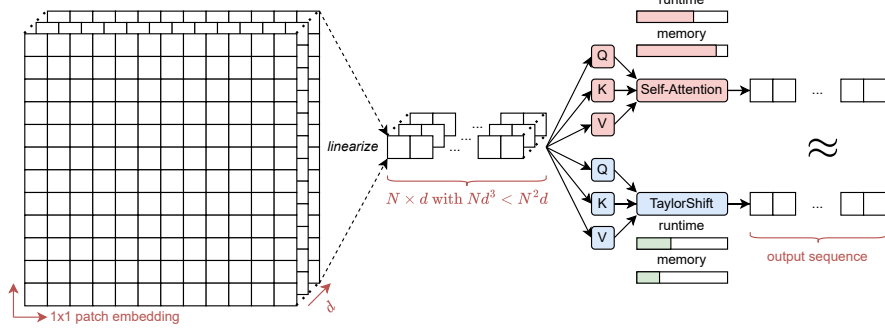


Fig. 2: TaylorIR has two pieces: (*left*) pixel-wise ( $1 \times 1$ ) patch embedding and (*right*) TaylorShift attention in place of windowed softmax attention. Together, they enable long-range context with lower memory and stable runtime.

**Efficient TaylorShift** For long sequences, we reorder the computation so that normalization happens *after* mixing with  $V$ . Define

$$\begin{aligned} Y_{\text{nom}} &= \left[ \mathbf{1} + QK^\top + \frac{1}{2}(QK^\top)^{\odot 2} \right] V, \\ Y_{\text{den}} &= \left[ \mathbf{1} + QK^\top + \frac{1}{2}(QK^\top)^{\odot 2} \right] \mathbf{1}_N, \end{aligned} \quad (5)$$

and return the elementwise normalized result  $Y = Y_{\text{nom}} \oslash Y_{\text{den}}$ , where  $\mathbf{1}_N$  is the length- $N$  vector of ones and  $\odot$  /  $\oslash$  denote Hadamard power and division.

To avoid building  $(QK^\top)^{\odot 2}$  explicitly, TaylorShift expands the squared term with a tensor-like operator  $\boxtimes : \mathbb{R}^{N \times d} \times \mathbb{R}^{N \times d} \rightarrow \mathbb{R}^{N \times d^2}$ ,

$$(QK^\top)^{\odot 2} V = (Q \boxtimes Q) (K \boxtimes K)^\top V, \quad (6)$$

so the constant and linear parts run in  $\mathcal{O}(Nd^2)$  and the squared part in  $\mathcal{O}(Nd^3)$ . In practice, Efficient TaylorShift is preferable once  $N$  is large (i.e., when  $Nd^3 \ll N^2d$  no longer holds).

### 3.2 Pixel-Wise Patch Embedding

Most ViT-based SR architectures reduce sequence length by partitioning the input into  $p \times p$  patches, typically with  $p \in \{4, 8\}$ . While this lowers computational cost, it implicitly enforces spatial smoothness within each patch and limits fine-grained control. TaylorIR instead adopts a degenerate patch size of  $p=1$ , embedding each pixel as an independent token. An image  $\mathbf{x} \in \mathbb{R}^{H \times W}$  is thus reshaped into a sequence  $\{\mathbf{x}_i\}_{i=1}^N$  with  $N=HW$ . This pixel-wise embedding exposes the full-resolution spatial manifold to the network, removes the hidden downsampling effect of large patches, and aligns naturally with the TaylorShift operator, which maintains tractable attention over long spatial windows.

Table 1: Quantitative comparison (average PSNR/SSIM) of our proposed TaylorSwinIR model, which applies TaylorIR to SwinIR, against state-of-the-art methods for classical image SR on benchmark datasets (Set5, Set14, BSD100, Urban100, and Manga109). As a result, TaylorSwinIR improves the performance of its underlying architecture, SwinIR, on most test sets.

Method	Scale	Training Dataset	Set5 [2]		Set14 [30]		BSD100 [15]		Urban100 [10]		Manga109 [16]	
			PSNR	SSIM	PSNR	SSIM	PSNR	SSIM	PSNR	SSIM	PSNR	SSIM
RCAN [33]	$\times 2$	DIV2K	38.27	0.9614	34.12	0.9216	32.41	0.9027	33.34	0.9384	39.44	0.9786
SAN [4]	$\times 2$	DIV2K	38.31	0.9620	34.07	0.9213	32.42	0.9028	33.10	0.9370	39.32	0.9792
IGNN [35]	$\times 2$	DIV2K	38.24	0.9613	34.07	0.9217	32.41	0.9025	33.23	0.9383	39.35	0.9786
HAN [23]	$\times 2$	DIV2K	38.27	0.9614	34.16	0.9217	32.41	0.9027	33.35	0.9385	39.46	0.9785
NLSA [17]	$\times 2$	DIV2K	38.34	0.9618	34.08	0.9231	32.43	0.9027	33.42	0.9394	39.59	0.9789
SwinIR [12]	$\times 2$	DIV2K	38.35	0.9620	34.14	0.9227	32.44	0.9030	33.40	0.9393	39.60	0.9792
<b>TaylorSwinIR (ours)</b>	$\times 2$	DIV2K	<b>38.46</b>	<b>0.9627</b>	<b>34.20</b>	<b>0.9235</b>	<b>32.49</b>	<b>0.9045</b>	<b>33.71</b>	<b>0.9417</b>	<b>39.70</b>	<b>0.9795</b>
RCAN [33]	$\times 3$	DIV2K	34.74	0.9299	30.65	0.8482	29.32	0.8111	29.09	0.8702	34.44	0.9499
SAN [4]	$\times 3$	DIV2K	34.75	0.9300	30.59	0.8476	29.33	0.8112	28.93	0.8671	34.30	0.9494
IGNN [35]	$\times 3$	DIV2K	34.72	0.9298	30.66	0.8484	29.31	0.8105	29.03	0.8696	34.39	0.9496
HAN [23]	$\times 3$	DIV2K	34.75	0.9299	30.67	0.8483	29.32	0.8110	29.10	0.8705	34.48	0.9500
NLSA [17]	$\times 3$	DIV2K	34.85	0.9306	30.70	0.8485	29.34	0.8117	29.25	0.8726	34.57	0.9508
SwinIR [12]	$\times 3$	DIV2K	34.89	0.9312	30.77	0.8503	29.37	0.8124	29.29	0.8744	34.74	0.9518
<b>TaylorSwinIR (ours)</b>	$\times 3$	DIV2K	<b>34.94</b>	<b>0.9317</b>	<b>30.79</b>	<b>0.8507</b>	<b>29.39</b>	<b>0.8145</b>	<b>29.47</b>	<b>0.8772</b>	<b>34.76</b>	<b>0.9521</b>
RCAN [33]	$\times 4$	DIV2K	32.63	0.9002	28.87	0.7889	27.77	0.7436	26.82	0.8087	31.22	0.9173
SAN [4]	$\times 4$	DIV2K	32.64	0.9003	28.92	0.7888	27.78	0.7436	26.79	0.8068	31.18	0.9169
IGNN [35]	$\times 4$	DIV2K	32.57	0.8998	28.85	0.7891	27.77	0.7434	26.84	0.8090	31.28	0.9182
HAN [23]	$\times 4$	DIV2K	32.64	0.9002	28.90	0.7890	27.80	0.7442	26.85	0.8094	31.42	0.9177
NLSA [17]	$\times 4$	DIV2K	32.59	0.9000	28.87	0.7891	27.78	0.7444	26.96	0.8109	31.27	0.9184
SwinIR [12]	$\times 4$	DIV2K	32.72	0.9021	28.94	0.7914	27.83	0.7459	<b>27.07</b>	<b>0.8164</b>	<b>31.67</b>	<b>0.9226</b>
<b>TaylorSwinIR (ours)</b>	$\times 4$	DIV2K	<b>32.74</b>	<b>0.9023</b>	<b>28.99</b>	<b>0.7917</b>	<b>27.83</b>	<b>0.7477</b>	27.06	0.8156	31.57	0.9225

### 3.3 Integrating TaylorIR into SwinIR

To evaluate compatibility with hierarchical backbones, we integrate TaylorIR into SwinIR, yielding TaylorSwinIR. While SwinIR already employs pixel embeddings, its attention is confined to non-overlapping  $w \times w$  windows, with  $w=8$  (i.e., 64 tokens). We extend the window size to  $w=48$  (i.e., 2304 tokens) and replace the original window attention  $\mathcal{A}_{\text{win}}$  with the TaylorShift attention  $\mathcal{A}_{\text{TS}}$ . Formally,

$$\mathbf{y} = \mathcal{A}_{\text{TS}}(\mathbf{Q}, \mathbf{K}, \mathbf{V}), \quad (7)$$

where  $\mathcal{A}_{\text{TS}}$  can operate either in its direct form for short sequences or in its efficient variant for long ones, depending on  $w^2$ . This substitution broadens the effective receptive field while keeping the asymptotic cost near-linear in  $N$ . Empirically, TaylorSwinIR preserves or improves reconstruction quality, reduces VRAM consumption at large window sizes, and remains fully drop-in compatible with SwinIR-style architectures.

## 4 Experiments

This section introduces our experiments conducted to assess the effectiveness of TaylorIR by applying it to SwinIR. First, we describe the setup and analyze the impact of the integration of TaylorIR. Next, we demonstrate how TaylorIR improves state-of-the-art transformer-based models on classical benchmarks and finally show how TaylorIR improves the contextual scope.

#### 4.1 Experimental Setup

We train all models on the DIV2K dataset [1], following the standard protocol of extracting  $192 \times 192$  RGB sub-images for training. Evaluation is performed on the benchmark datasets Set5 [2], Set14 [30], BSDS100 [15], Manga109 [16], and Urban100 [10]. We report results for upscaling factors of  $\times 2$ ,  $\times 3$ , and  $\times 4$ , using PSNR and SSIM on the luminance channel of the YCbCr space for fair comparison with prior work.

#### 4.2 State-of-the-Art Comparison

To demonstrate the effectiveness of TaylorSwinIR in classical image SR benchmarks, we compare it against prominent state-of-the-art models including RCAN [33], RRDB [27], SAN [5], IGNN [36], HAN [24], NLSA [18], and the baseline SwinIR model [12]. Evaluations were conducted across multiple datasets (Set5, Set14, BSD100, Urban100, and Manga109) and scaling factors ( $\times 2$ ,  $\times 3$ , and  $\times 4$ ) to ensure comprehensive analysis. Results are shown in Table 1.

TaylorSwinIR consistently outperforms SwinIR across most datasets, particularly at lower scaling factors ( $\times 2$  and  $\times 3$ ), highlighting the advantage of pixel-wise embeddings combined with TaylorShift attention. On Urban100 at  $\times 2$ , TaylorSwinIR achieves a PSNR gain of **+0.31 dB** over SwinIR, demonstrating its improved ability to reconstruct fine, high-frequency structures common in urban imagery. Similarly, on Manga109 at  $\times 2$ , it reaches **39.70 dB** PSNR versus **39.60 dB** for SwinIR, reflecting superior detail preservation in dense line-art textures. Across all benchmarks and scales, TaylorSwinIR yields PSNR improvements ranging from **+0.02** to **+0.31 dB**, accompanied by consistent SSIM gains, confirming the stability of its enhancements. At  $\times 4$  magnification, TaylorSwinIR maintains parity with SwinIR on most datasets, indicating that the efficiency-oriented TaylorShift mechanism does not compromise reconstruction fidelity at higher scales.

In summary, TaylorSwinIR establishes a new benchmark among transformer-based SR models by jointly delivering high perceptual fidelity and computational efficiency. Beyond its performance gains, the core advantage of **TaylorIR** lies in its *plug-and-play* design: it can be seamlessly integrated into existing attention-based architectures without architectural modifications. This modularity enables straightforward adoption across diverse SR frameworks. Together, these results position TaylorIR as a flexible and scalable foundation for future high-quality image SR systems.

#### 4.3 Qualitative Results

In Figure 3, Figure 4 and Figure 5, we present visual comparisons across different scaling factors ( $\times 2$ ,  $\times 3$ , and  $\times 4$ ) between the benchmark model SwinIR and our proposed TaylorSwinIR approach. Notably, in Figure 4, TaylorSwinIR demonstrates clear improvements at the  $\times 3$  scale for the Manga109 image, *MiraiSan*, where it produces significantly sharper and more detailed results.



Fig. 3: **Visual comparison on 2 $\times$  SR.** Red boxes in the HR images mark the regions shown for comparison. On (left) Urban100 image img\_044, TaylorSwinIR achieves 44.87 dB / 0.9921 versus SwinIR’s 44.13 dB / 0.9905. On (right) Urban100 image img\_009, TaylorSwinIR achieves 42.65 dB / 0.9834 versus SwinIR’s 42.20 dB / 0.9834.



Fig. 4: **Visual comparison on 3 $\times$  SR.** Yellow and red boxes in the HR images indicate the regions shown for comparison. On (left) Manga109 image AosugiruHaru, TaylorSwinIR achieves **44.30 dB / 0.9898** versus SwinIR’s 44.15 dB / 0.9896. On (right) image HaruichibanNoFukukoro, TaylorSwinIR attains **42.79 dB / 0.9872** compared to SwinIR’s 42.47 dB / 0.9870.

TaylorSwinIR consistently achieves subjectively comparable or superior image quality relative to SwinIR across all tested scales. These gains are attributed to the expanded receptive field, which enhances the model’s ability to capture richer contextual information. Additionally, TaylorSwinIR demonstrates optimized memory efficiency, which not only supports high-quality image reconstruction but also makes it more computationally viable. This combination of improved super-resolution quality and reduced memory consumption highlights TaylorSwinIR as an effective and resource-efficient solution for detailed image enhancement.



Fig. 5: **Visual comparison on 4× SR.** Red boxes in the HR images indicate the cropped regions for comparison. On (left) Urban100 image img\_090, TaylorSwinIR achieves **40.54 dB / 0.9836** versus SwinIR’s 40.34 dB / 0.9832. On (right) image img\_081, TaylorSwinIR reaches **39.81 dB / 0.9807** compared to SwinIR’s 39.80 dB / 0.9802.

#### 4.4 Analysis of Self-Attention vs. TaylorShift

We analyze how large window sizes and attention mechanisms affect runtime and memory. To control for context, we fix the window at  $48 \times 48$  and compare *SwinIR (fine)* with *TaylorSwinIR* (TaylorShift). For reference, we also report the throughput of the default *SwinIR (original)* with  $8 \times 8$  windows, noting that it uses a different window size.

**Impact on Memory Efficiency (VRAM)** At the same  $48 \times 48$  window size, *TaylorSwinIR* consistently uses less VRAM than *SwinIR (fine)* across datasets, with observed reductions ranging from roughly 37% to 85%, as shown in Figure 6. For example, on Urban100, memory drops from 78.5 GB to 49.1 GB. These savings enable large-window inference under tighter hardware budgets and make wide-context SR more practical at scale.

**Impact on Computational Complexity (Throughput)** With  $8 \times 8$  windows, *SwinIR (original)* reaches 6.12 images/s due to small local windows and low attention cost. At matched large windows ( $48 \times 48$ ), *SwinIR (fine)* runs at 0.123 images/s, while *TaylorSwinIR* attains 0.124 images/s under the same setting. Although the absolute gain is modest at  $48 \times 48$ , TaylorShift’s scaling becomes increasingly favorable as sequence length grows, mitigating the quadratic sensitivity of standard windowed self-attention to window area.

**Practical Trade-Offs** Large windows expand contextual reasoning but stress throughput and memory. TaylorShift preserves most of the runtime characteristics at  $48 \times 48$  while substantially lowering the memory footprint, offering a more deployable path to large-context SR. In practice, this plug-and-play swap of the window attention with TaylorShift amortizes costs as resolution and context grow, without altering the backbone architecture.

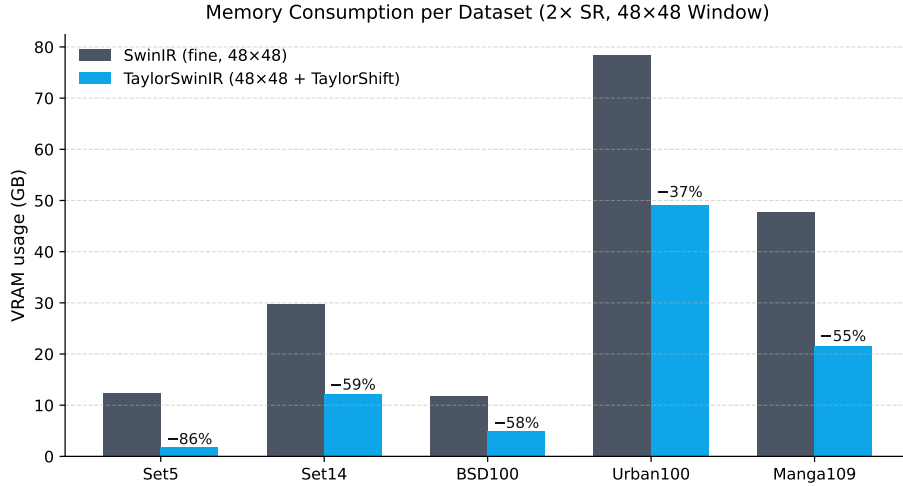


Fig. 6: **Memory consumption** for  $2\times$  SR at  $48\times 48$  windows. TaylorSwinIR ( $48\times 48 + \text{TaylorShift}$ ) substantially reduces VRAM usage compared to SwinIR (fine,  $48\times 48$ ) across datasets, with per-dataset savings annotated above the bars (percentage reduction vs. SwinIR (fine)).

#### 4.5 Contextual Scope

Figure 7 demonstrates the main advantages of TaylorIR underlying its improved reconstruction quality: the extended contextual scope. We demonstrate this by visualizing Local Attention Maps (LAM) [8] at a scaling of  $2\times$  and  $4\times$ . Unlike the unmodified SwinIR, which is restricted by its smaller window field, TaylorIR enables a broader diffusion of contextual information while keeping memory consumption low, as shown in the previous Sections. This results in an expanded Local Attention Map, where a higher diffusion index showcases a greater spread of information used for reconstruction across relevant areas within the image.

## 5 Limitations & Future Work

While TaylorIR demonstrates enhanced memory efficiency and performance in image super-resolution, several limitations remain. Although TaylorShift attention significantly reduces computational complexity, the computation still face substantial memory demands for extremely high-resolution images.

Future work could explore hybrid models that combine the strengths of convolutional and transformer architectures to improve performance across diverse image types. Another promising direction would be the optimization of TaylorIR for real-time applications on edge devices by incorporating quantization and model compression techniques.

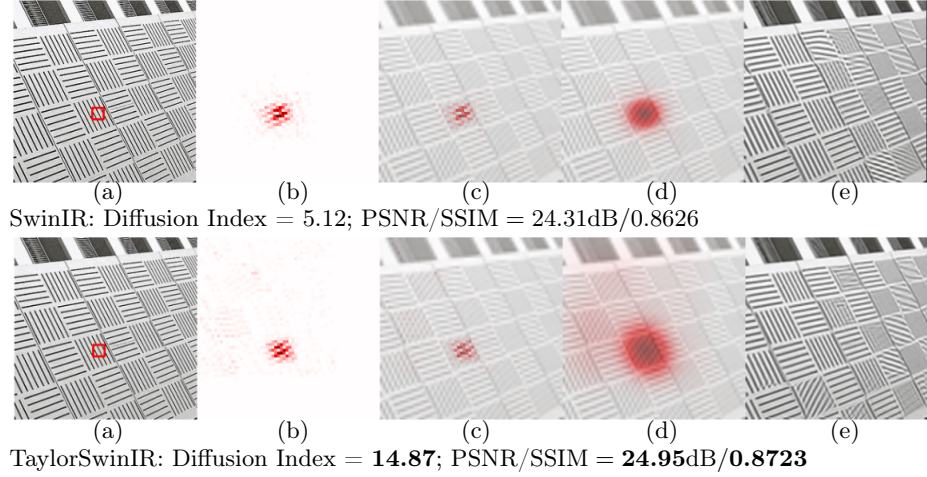


Fig. 7: Comparison of Local Attention Maps (LAM) [8] between SwinIR and TaylorSwinIR for 2x (**top**) and 4x (**bottom**) image SR. From left to right, the images show: (a) The original image with a selected region highlighted (red boxes), (b) the LAM visualization, (c) the LAM result overlaid on the input image, (d) the informative area overlaid on the input image, and (e) the final super-resolved output image. Overall, TaylorIR leads to a higher diffusion index, which shows its extended contextual scope and improved image quality metrics compared to SwinIR without TaylorIR.

## 6 Conclusion

In this work, we introduced TaylorIR, a method to extend transformer-based SR models by replacing the standard self-attention mechanism with TaylorShift attention and enabling long sequences, primarily through  $1 \times 1$  patch embeddings, to be processed faster and significantly more memory efficient. More specifically, our proposed method allowed us to scale up SwinIR with a  $48 \times 48$  window, resulting in a sequence length of 2304, capturing more global context, which leads to enhanced image quality while maintaining memory efficiency - a feat unattainable with traditional attention mechanisms. TaylorSwinIR, the TaylorIR-extended SwinIR architecture, achieves superior PSNR and SSIM scores across classical test benchmarks like Set5, Set14, BSD100, Urban100, and Manga109, surpassing state-of-the-art models, including SwinIR. This reduced memory footprint is particularly meaningful for deploying SR transformers in resource-constrained environments, bringing high-quality SR closer to real-time applications.

## 7 Societal Impact

While using long sequences in image SR enables enhanced detail and quality, it also introduces significant computational complexity and memory consumption. Although our proposed method, TaylorIR, reduces these demands, the resources required remain substantial. Continued improvements in efficiency are crucial to minimize the environmental footprint associated with high-performance computing, and this needs to be addressed in future work.

## Acknowledgements

This work was supported by the BMBF projects SustainML (Grant 101070408), Albatross (Grant 01IW24002) and by Carl Zeiss Foundation through the Sustainable Embedded AI project (P2021-02-009).

## References

1. Agustsson, E., Timofte, R.: Ntire 2017 challenge on single image super-resolution: Dataset and study. In: CVPRW. pp. 126–135 (2017)
2. Bevilacqua, M., Roumy, A., Guillemot, C., Alberi-Morel, M.L.: Low-complexity single-image super-resolution based on nonnegative neighbor embedding (2012)
3. Chen, X., Wang, X., Zhou, J., Qiao, Y., Dong, C.: Activating more pixels in image super-resolution transformer. In: CVPR. pp. 22367–22377 (2023)
4. Dai, T., Cai, J., Zhang, Y., Xia, S.T., Zhang, L.: Second-order attention network for single image super-resolution. In: CVPR. pp. 11065–11074 (2019)
5. Dai, T., Cai, J., Zhang, Y., Xia, S.T., Zhang, L.: Second-order attention network for single image super-resolution. In: CVPR. pp. 11065–11074 (2019)
6. Dosovitskiy, A.: An image is worth 16x16 words: Transformers for image recognition at scale. arXiv preprint arXiv:2010.11929 (2020)

7. Dosovitskiy, A., Beyer, L., Kolesnikov, A., Weissenborn, D., Zhai, X., Unterthiner, T., Dehghani, M., Minderer, M., Heigold, G., Gelly, S., Uszkoreit, J., Houlsby, N.: An image is worth 16x16 words: Transformers for image recognition at scale. CoRR **abs/2010.11929** (2020), <https://arxiv.org/abs/2010.11929>
8. Gu, J., Dong, C.: Interpreting super-resolution networks with local attribution maps. In: CVPR. pp. 9199–9208 (2021)
9. Guo, T., Seyed Mousavi, H., Huu Vu, T., Monga, V.: Deep wavelet prediction for image super-resolution. In: CVPRW. pp. 104–113 (2017)
10. Huang, J.B., Singh, A., Ahuja, N.: Single image super-resolution from transformed self-exemplars. In: CVPR. pp. 5197–5206 (2015)
11. Li, J., Pei, Z., Li, W., Gao, G., Wang, L., Wang, Y., Zeng, T.: A systematic survey of deep learning-based single-image super-resolution. ACM Computing Surveys **56**(10), 1–40 (2024)
12. Liang, J., Cao, J., Sun, G., Zhang, K., Van Gool, L., Timofte, R.: Swinir: Image restoration using swin transformer. In: CVPR. pp. 1833–1844 (2021)
13. Lim, B., Son, S., Kim, H., Nah, S., Mu Lee, K.: Enhanced deep residual networks for single image super-resolution. In: CVPRW. pp. 136–144 (2017)
14. Liu, P., Zhang, H., Lian, W., Zuo, W.: Multi-level wavelet convolutional neural networks. IEEE Access **7**, 74973–74985 (2019)
15. Martin, D., Fowlkes, C., Tal, D., Malik, J.: A database of human segmented natural images and its application to evaluating segmentation algorithms and measuring ecological statistics. In: ICCV. vol. 2, pp. 416–423. IEEE (2001)
16. Matsui, Y., Ito, K., Aramaki, Y., Fujimoto, A., Ogawa, T., Yamasaki, T., Aizawa, K.: Sketch-based manga retrieval using manga109 dataset. Multimedia Tools and Applications **76**(20), 21811–21838 (2017)
17. Mei, Y., Fan, Y., Zhou, Y.: Image super-resolution with non-local sparse attention. In: CVPR. pp. 3517–3526 (2021)
18. Mei, Y., Fan, Y., Zhou, Y.: Image super-resolution with non-local sparse attention. In: CVPR. pp. 3517–3526 (2021)
19. Moser, B.B., Frolov, S., Raue, F., Palacio, S., Dengel, A.: Dwa: Differential wavelet amplifier for image super-resolution. In: International Conference on Artificial Neural Networks. pp. 232–243. Springer (2023)
20. Moser, B.B., Raue, F., Frolov, S., Palacio, S., Hees, J., Dengel, A.: Hitchhiker’s guide to super-resolution: Introduction and recent advances. IEEE TPAMI **45**(8), 9862–9882 (2023)
21. Moser, B.B., Shanbhag, A.S., Raue, F., Frolov, S., Palacio, S., Dengel, A.: Diffusion models, image super-resolution, and everything: A survey. IEEE Transactions on Neural Networks and Learning Systems (2024)
22. Nauen, T.C., Palacio, S., Dengel, A.: Taylorshift: Shifting the complexity of self-attention from squared to linear (and back) using taylor-softmax. arXiv preprint arXiv:2403.02920 (2024)
23. Niu, B., Wen, W., Ren, W., Zhang, X., Yang, L., Wang, S., Zhang, K., Cao, X., Shen, H.: Single image super-resolution via a holistic attention network. In: ECCV. pp. 191–207 (2020)
24. Niu, B., Wen, W., Ren, W., Zhang, X., Yang, L., Wang, S., Zhang, K., Cao, X., Shen, H.: Single image super-resolution via a holistic attention network. In: ECCV. pp. 191–207. Springer (2020)
25. Vaswani, A.: Attention is all you need. NeurIPS (2017)
26. Vu, A.D., Nguyen, K.V., Bui, B.Q., Kamel, N.: A comprehensive survey of super-resolution remote sensing image datasets: Evolution, challenges, and future directions. IEEE Access (2025)

27. Wang, X., Yu, K., Wu, S., Gu, J., Liu, Y., Dong, C., Qiao, Y., Change Loy, C.: Esrgan: Enhanced super-resolution generative adversarial networks. In: ECCV. pp. 0–0 (2018)
28. Xiao, H., Yang, Z., Liu, T., Liu, S., Huang, X., Dai, J.: Deep learning for medical imaging super-resolution: A comprehensive review. *Neurocomputing* p. 129667 (2025)
29. Zamir, S.W., Arora, A., Khan, S., Hayat, M., Khan, F.S., Yang, M.H.: Restormer: Efficient transformer for high-resolution image restoration. In: CVPR. pp. 5728–5739 (2022)
30. Zeyde, R., Elad, M., Protter, M.: On single image scale-up using sparse-representations. In: International conference on curves and surfaces. pp. 711–730. Springer (2010)
31. Zhang, D., Huang, F., Liu, S., Wang, X., Jin, Z.: Swinir: Revisiting the swinir with fast fourier convolution and improved training for image super-resolution. arXiv preprint arXiv:2208.11247 (2022)
32. Zhang, Y., Li, K., Li, K., Wang, L., Zhong, B., Fu, Y.: Image super-resolution using very deep residual channel attention networks. In: ECCV. pp. 286–301 (2018)
33. Zhang, Y., Li, K., Li, K., Wang, L., Zhong, B., Fu, Y.: Image super-resolution using very deep residual channel attention networks. In: ECCV. pp. 286–301 (2018)
34. Zhang, Y., Tian, Y., Kong, Y., Zhong, B., Fu, Y.: Residual dense network for image super-resolution. In: CVPR. pp. 2472–2481 (2018)
35. Zhou, S., Zhang, J., Zuo, W., Loy, C.C.: Cross-scale internal graph neural network for image super-resolution. arXiv preprint arXiv:2006.16673 (2020)
36. Zhou, S., Zhang, J., Zuo, W., Loy, C.C.: Cross-scale internal graph neural network for image super-resolution. *NeurIPS* **33**, 3499–3509 (2020)